communications earth & environment

Article

A Nature Portfolio journal

https://doi.org/10.1038/s43247-025-02322-0

Late Miocene greening of the Peruvian Desert

Check for updates

Diana Ochoa [1,2], Matthieu Carré [2,3], Juan-Felipe Montenegro[2], Thomas J. DeVries[4], Dayenari Caballero-Rodríguez[5], Oris Rodríguez-Reyes[5,6], Angel Barbosa-Espitia[7], Jorge Cardich [2], Edgar Cruz-Acevedo [2,8], Danilo Cruz[9], David A. Foster [9], María LaTorre-Acuy[10], Franco Quispe[2], María Rivera-Chira[2], Pedro E. Romero[11], Rodolfo Salas-Gismondi [2,12], Mario Urbina[12] & José-Abel Flores [1]

The response of the hyperarid Pacific coast of South America to greenhouse warming remains highly uncertain but has profound implications for the future habitability of the region. Here, we present the first paleobotanical study documenting the Peruvian Desert's response to the Late Miocene greenhouse climate, when radiative forcing was comparable to 21st century projections. Fossil leaves, wood, and pollen from the Pisco Formation lagerstätte indicate a diverse dry forest biome where an absolute desert is observed today. Rainfall at 8–6 Ma is estimated to have been three times higher than today, possibly due to a warmer Eastern Tropical Pacific Ocean or to more frequent El Niño events. Our results suggest that the impacts of tropical climate dynamical changes on ecosystems of the Pacific South American coast under greenhouse warming conditions may outweigh those of heat and evaporation, potentially enabling vegetation expansion, biome transformations, and enhanced habitability in this region.

Predictions suggest an intensifying global evaporation-minus-precipitation pattern due to ongoing global warming, implying an overall trend of increasing aridity in already dry regions[1]. For the Atacama Desert, greenhouse warming projections suggest a 15–30% decrease in rainfall by the end of the 21st century[2]. Despite this, El Niño Southern Oscillation (ENSO) is expected to continue delivering intense rainfall events and storms to this arid region[2,3]. However, the future behavior of ENSO and the tropical Pacific circulation remains a subject of debate[4,5], creating uncertainty about their impact on South America. Strong model biases in the South-Eastern Pacific[6,7], uncertainty in South American monsoon simulations[8,9], and long-term vegetation feedbacks on regional hydrology influenced by CO_2 physiological effects[10] further add complexity to predictions about the future of the arid Pacific coast of South America—stretching from the northern Peruvian coast to Argentinean Patagonia—and its habitability. Here, we present a unique paleontological record from the Coastal Peruvian Desert (Fig. 1), arguably the northern extension of the Atacama Desert, preserved from the Late Miocene (8 to 6 million years ago (Ma)). With atmospheric pCO_2 levels estimated between 350 and 450 ppm, this period of global warmth is considered, to some extent, as a useful analog for an equilibrated greenhouse climate[11,12].

The Peruvian coast ranks today among the Earth´s driest regions (annual $P < 15$ mm)[13], with fragmented ecosystems and vast landscapes devoid of vascular plants. This hyperaridity results from the combined influence of the southeastern Pacific anticyclone and the Andean cordillera[14]. Coastal winds driven by the anticyclone and latitudinal surface temperature gradients promote the upwelling of cool subsurface waters along the South-American Pacific coast, suppressing atmospheric convection[15]. The Andes Mountains further contribute to extreme aridity by creating a rain-shadow effect that limits westward moisture advection from the Amazon and the Atlantic[14]. However, modeling studies with reduced Andes heights[16,17] and wet episodes during the Plio-Pleistocene, evidenced by large wetland and lake deposits[18,19], suggest that global radiative forcing

[1]Departamento de Geología, Universidad de Salamanca, Salamanca, Spain. [2]Centro de Investigación para el Desarrollo Integral y Sostenible (CIDIS), Facultad de Ciencias e Ingeniería, Universidad Peruana Cayetano Heredia (UPCH), Lima, Peru. [3]LOCEAN-IPSL, Laboratoire d'Océanographie et du Climat: Expérimentation et Approches Numériques, Sorbonne Université/CNRS/IRD/MNHN, Paris, France. [4]The Burke Museum, University of Washington, Seattle, WA, USA. [5]Smithsonian Tropical Research Institute, Panama, Panama. [6]Facultad de Ciencias Naturales, Exactas y Tecnología, Universidad de Panamá, Panama, Panama. [7]Programa de Geografía, Universidad Nacional de Colombia, La Paz, Colombia. [8]Departamento de Ciencias Exactas y Desarrollo Humano, Facultad de Ciencias Biológicas, Universidad Autónoma de Nuevo León, Nuevo León, Mexico. [9]Department of Geological Sciences, University of Florida, Gainesville, FL, USA. [10]Herbario Nacional, Universidad Nacional Mayor de San Marcos, Lima, Peru. [11]Facultad de Ciencias Biológicas, Universidad Nacional Mayor de San Marcos, Lima, Peru. [12]Departamento de Paleontología de Vertebrados, Museo de Historia Natural, Universidad Nacional Mayor de San Marcos, Lima, Peru. e-mail: diana.ochoa@usal.es

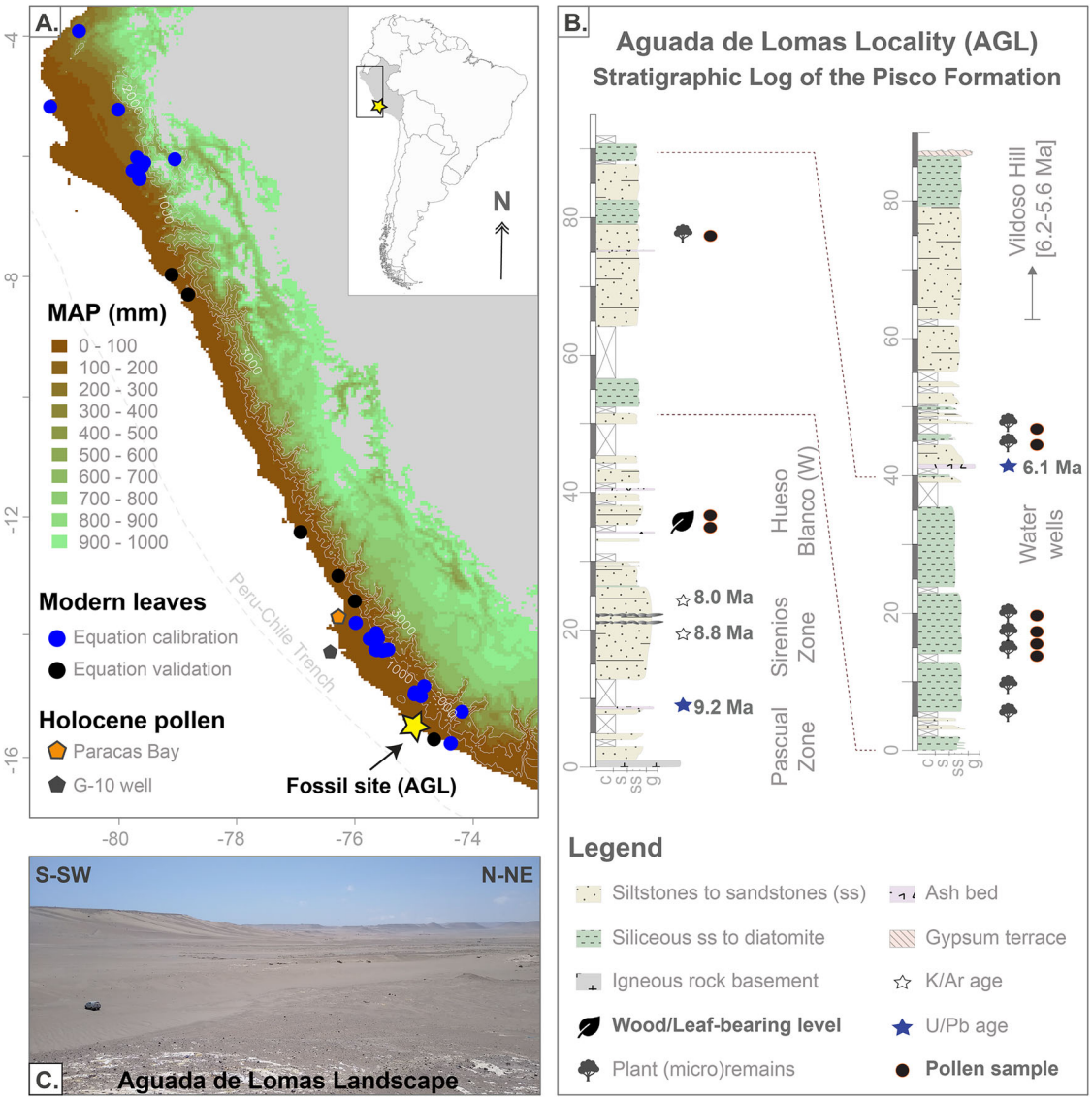

Fig. 1 | Fossil site location and stratigraphic position. A Mean annual precipitation (MAP) along the Peruvian western Andean slopes, showing location of the Late Miocene fossil site (yellow filled star), Holocene pollen samples from Paracas Bay and the G-10 core (pentagon), and modern leaf herbarium samples (circles) used for recalibrating and validating MAP equations. **B** Simplified lithostratigraphic log for the Pisco sediments at the Aguada de Lomas Locality (AGL), indicating existing chronostratigraphic framework for the AGL, as well as stratigraphic position of studied pollen samples (solid circles), wood and leaf-bearing bed (leaf icon), and U-Pb dated ash layers (solid blue stars). c clay, s silt, ss sandstone, g gravel. **C** Panoramic view of the present-day landscape at the Aguada de Lomas Locality.

and regional atmospheric circulation play a more significant role in shaping the area's precipitation regime[20]. Thus, the region´s extreme aridity is rooted in both its geological and oceanographic characteristics, but is heavily influenced by regional atmospheric dynamics[16,17,21].The onset of hyperaridity and the process that drove the desertification of western South America remain highly controversial. One hypothesis proposes that hyperaridity started when the Andes reached ~2500 m height during the Middle Miocene uplift phase (12–10 Ma)[22–24]. However, estimates for the onset of Atacama hyperaridity in Chile range from the late Jurassic to the Late Pliocene[25–27], a large uncertainty reflecting the diversity of geomorphological and geochemical indicators, and the complexity of interpretations[28,29]. A well-constrained paleoclimate record from the hyperarid Peruvian coast, arguably the northern extension of the Atacama, could offer insights into the region's climate evolution. However, this history remains virtually unknown. Understanding past climate and biome dynamics during the Neogene greenhouse period is also critical for assessing the future habitability of this region, now home to ~17 million people.

We present a palynological and paleobotanical Miocene record from the Coastal Peruvian Desert (15.5°S; 74.8°W; Fig. 1), which offers rare insights into a region primarily known through marine deposits. Fossil leaves, wood fragments, and palynological samples (Fig. 2), dating from 8 to 6 Ma, were recovered from the Pisco Formation ("Methods," Supplementary Figs. 1, 2). These fossils provide direct evidence of Late Miocene coastal biomes. The Pisco Formation, in part, composed of shoreface to inner shelf sediments deposited in semi-protected bays along the Peruvian shelf[30], is renowned for the excellent preservation of marine vertebrates[31–33]. The chronology of the 200 m thick sedimentary sequence at the locality Aguada de Lomas (AGL), where botanical fossils were collected, is controlled by biostratigraphy and four stratigraphically consistent radiometric ages ("Methods"; Supplementary Figs. 1, 2). Through palynological and paleobotanical analyses (Supplementary Figs. 3–5), leaf-based precipitation estimates (Supplementary Fig. 6), and evaluation of climatic niches (Supplementary Figs. 7, 9), we discuss the response of western South American coastal biomes and climate to the Late Miocene greenhouse conditions. Our

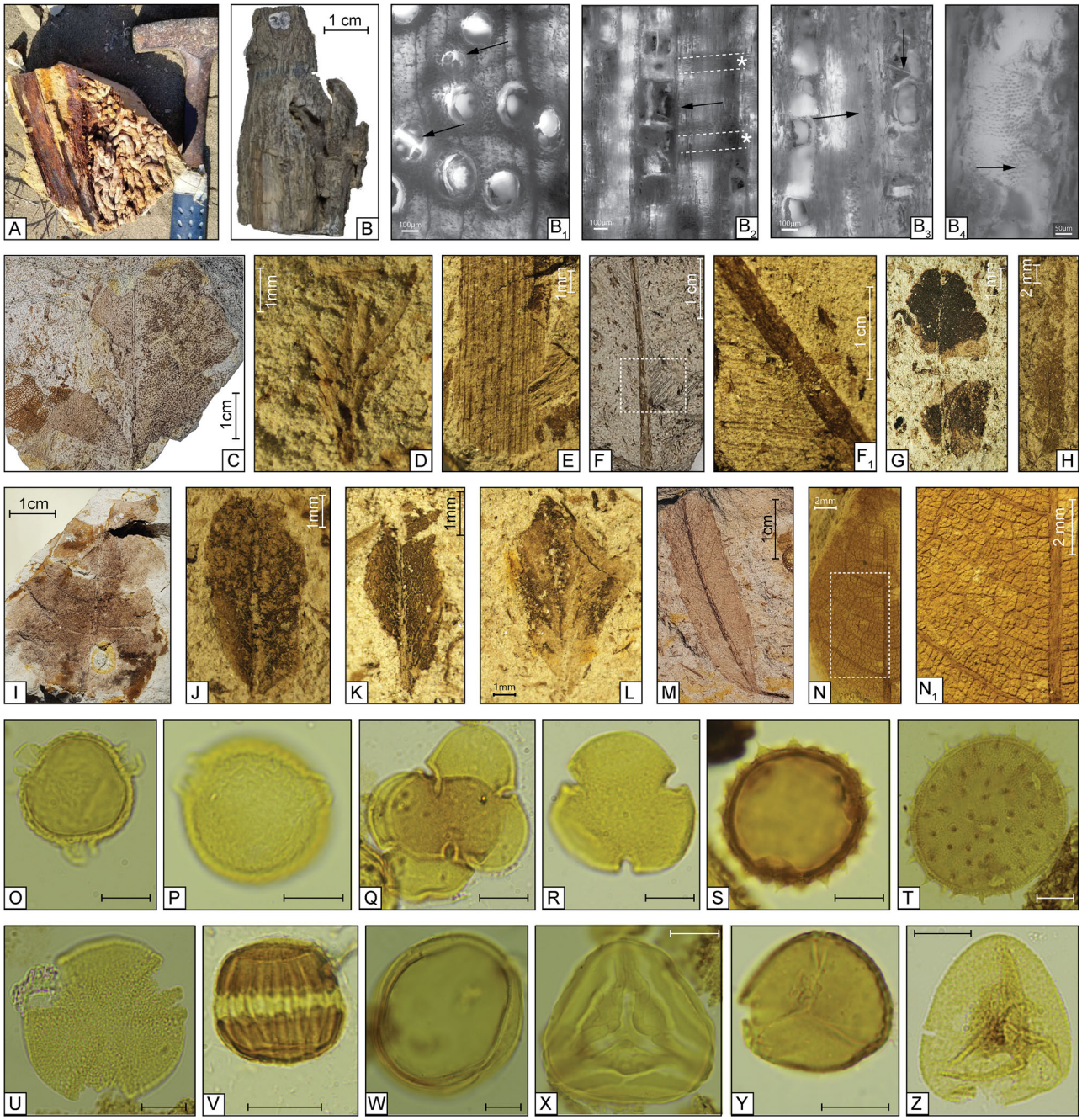

Fig. 2 | Late Miocene fossil leaves, wood, and palynomorphs from the Pisco Formation. A Wood fragment with *Teredolites*. **B** Silicified wood anatomy of *Neltuma* (ex *Prosopis*). **B_1** Cross-sectional view showing axial parenchyma vasicentric and confluent with sclerotic tyloses (arrows). **B_2** Radial longitudinal section with procumbent cells and sclerotic tyloses. **B_3** Tangential longitudinal section with 4 to 10 seriate and short vessel element length. **B_4** Alternate and small intervessel pits. **C–P** Selected macrofossil plant remains. **C** Undetermined leaves as found in the field. **D** Poaceae flower. **E** Poaceae. **F–F_1** Arecaceae. **F_1** closeup of (**F**). **G** Rosaceae (Sanguisorbeae, possibly *Polylepis*). **H** Salicaceae *(Salix* cf. *humboldtiana*). **I–L** Undetermined leaves. **M** Myrtaceae. **N-N_1** Capparaceae (*Capparis*). **N_1** closeup of (**N**). **O–Z** Selected Late Miocene palynomorphs. Scale bars for palynomorphs is 10 µm. **O**, **P** *Polylepis-Acaena*. **Q** *Bombacidites sp.1*, Malvaceae. **R** *Bombacidites sp.2*, Malvaceae. **S** *Malvacipolloides maristellae;* Malvaceae. **T** *Echiperiporites germeraadii.* **U** Caesalpinoid (Fabaceae). **V** Polygalaceae. **W** Araceae. **X** *Ceratopteris sp.* **Y** cf. *Huperzia*. **Z** *Granulatisporis sp.*

results offer new perspectives on rainfall patterns in a warmer world, while contributing to the assessment of regional boundary conditions, data/model calibrations, and continental climate variability.

Fossil evidence for a vegetated desert in the Late Miocene

The plant macrofossils, comprising 55 fossil leaves and three wood fragments, include the genera *Capparis*, *Salix* (cf. *humboldtiana*), and members of the Myrtaceae, Rosaceae (Sanguisorbeae?), Asteraceae, Poaceae, and Arecaceae families (Fig. 2; Supplementary Data S2). The leaves are predominantly non-monocotyledonous, featuring entire margins (53.8%), acute apices (30.8%), and nanophyll leaf sizes (32.7%, range: 25–225 mm^2). Silicified wood indicates the presence of drought-resistant *Neltuma* (ex *Prosopis*) trees (Fig. S5; Supplementary Data S4). Nine well-preserved palynological samples show a diverse Late Miocene assemblage, dominated by *Polylepis-Acaena* (35.4%), various Asteraceae morphotypes (19.1%), and the evergreen *Podocarpus* (2.6%) (Fig. 2; Supplementary Data S2).

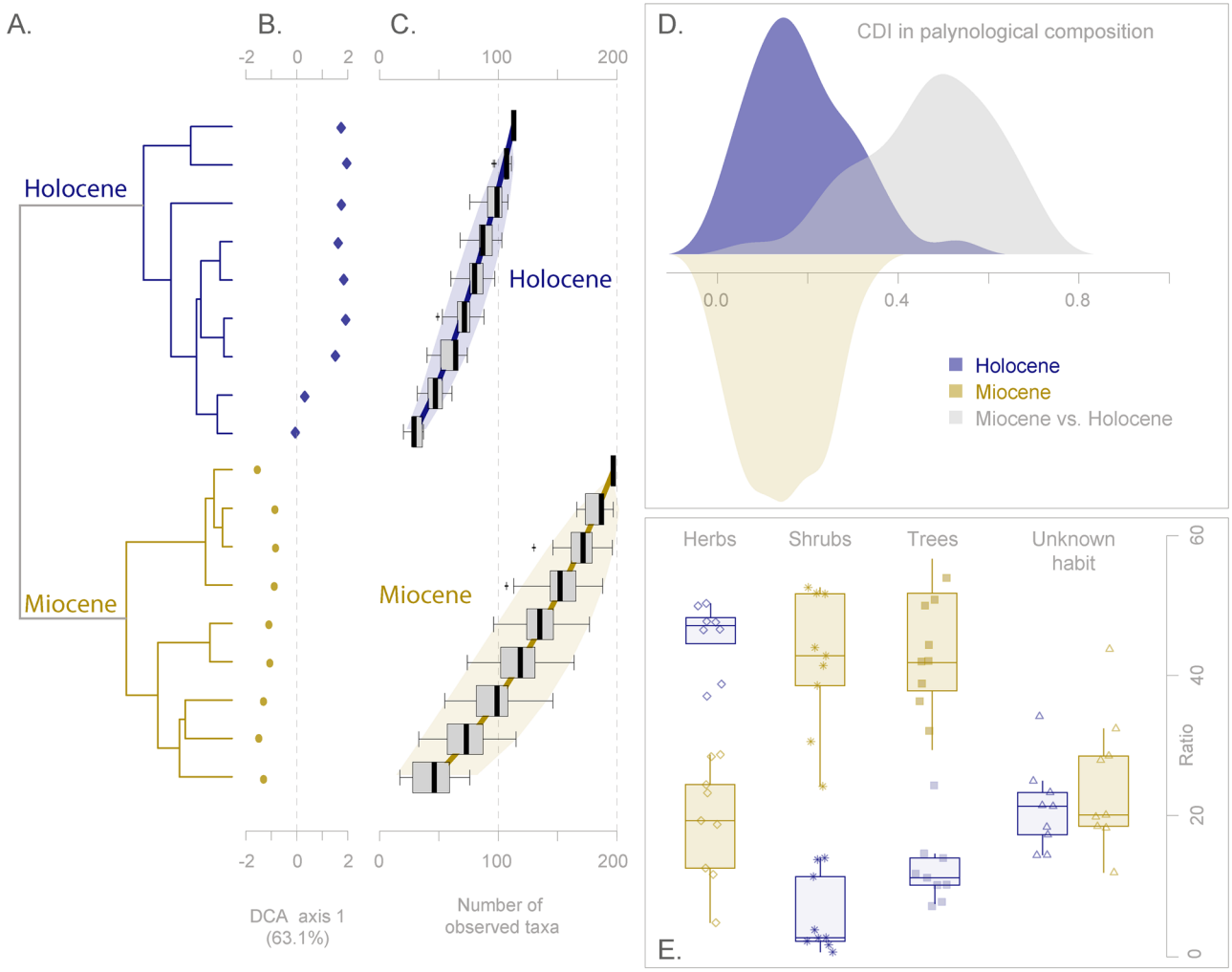

Fig. 3 | Diversity and compositional comparison of Miocene and Holocene palynological assemblages. **A** Coniss Cluster showing two distinct clusters, Miocene (yellow) and Holocene (blue). **B** First DCA axis, note Miocene samples are distinct from Holocene ones. **C** Species accumulation curves per period, boxplots indicate a range of accumulated number of individuals as samples are added to the sample pool. **D** Chao Dissimilarity Index (CDI) within Miocene (yellow) and Holocene (blue) palynofloras, and dissimilarities between both groups (gray). **E** Pollen-inferred plant habits. Note significant differences on herbs (p value: 4.114e-05; $w = 0$), shrubs (p value: 4.114e-05; $w = 81$), and trees (p value: 4.114e-05; $w = 81$).

These terrestrial macrofossils, found within shallow-marine sediments (Supplementary Figs. 1, 2), could have been transported from the Andes by rivers. However, the associated sedimentary facies show no evidence of alluvial, fluvial, or estuarine deposits (Supplementary Figs. 1, 2), nor have any relict geomorphological features of fluvial transport or riverine incision been identified in the area[30,32,34]. The well-preserved state of the fossil leaves precludes a long-distance fluvial transport, and longshore currents as a long-distance transport mechanism are also unlikely, given the relatively protected embayment of the coast at that time[30,33], suggesting a local origin for the fossil leaves. While long-distance pollen deposition is possible, the prevalence of *Polylepis-Acaena* grains (over 30%), which have weak dispersal and limited deposition[35], further supports a local origin for at least the *Polylepis-Acaena* component of the pollen record. This new fossil record very likely provides direct evidence of vegetation cover in the Late Miocene lowlands, where a non-vegetated landscape exists today (Fig. 2A).

A diverse yet non-analogous flora

The fossil palynoflora was compared against Holocene pollen assemblages to assess the characteristics of past vegetation. Nine Holocene samples [0–9.6 ky B.P.], collected from sedimentary settings similar to those of the Pisco Formation, served as a modern vegetation benchmark (Fig. 1; Supplementary Figs. 3, 4; "Methods"). The modern pollen assemblage, primarily wind-transported, reflects a flora dominated by alders (*Alnus*), grasses (Poaceae), sedges (Cyperaceae), goosefoot (Chenopodioideae, Amaranthaceae), and asters (Asteraceae). We found no significant variance in species abundance distribution within assemblages (p value = 0.22, df = 9.56; Fig. S3). However, Miocene palynoflora showed significantly higher diversity, both within-sample and standing, compared to the Holocene (Fig. 3; p value = 0.030, df = 4.1; Supplementary Fig. 3; Supplementary Data S2), along with distinct compositional differences (Fig. 3).

In addition to a higher diversity, the Miocene palynoflora exhibits a higher proportion of *Polylepis-Acaena* (35.4%), alongside *Podocarpus* trees, palms, bromeliads, cactoids, caesalpinoids, bombacoids, and ferns. This contrasts with the herbaceous-dominated Holocene assemblage (Fig. 3E; Supplementary Data S2), characterized by grasses, sedges, goosefoot, and asters, typical of short-cycle annual successions[36–38]. We interpret the presence of *Alnus* (7.2%), a pioneer and prolific pollen producer, as evidence of wind transport from Holocene Andean biomes. The prevalence of trees and shrubs is further supported by the discovery of *Neltuma* (ex *Prosopis*) silicified wood (Supplementary Fig. 5) and leaves from *Capparis*, *Salix*, and Myrtaceae. The assemblage from this paleobotanical record starkly contrasts with the modern flora and the xeric landscape of the Coastal Peruvian Desert[36–38].

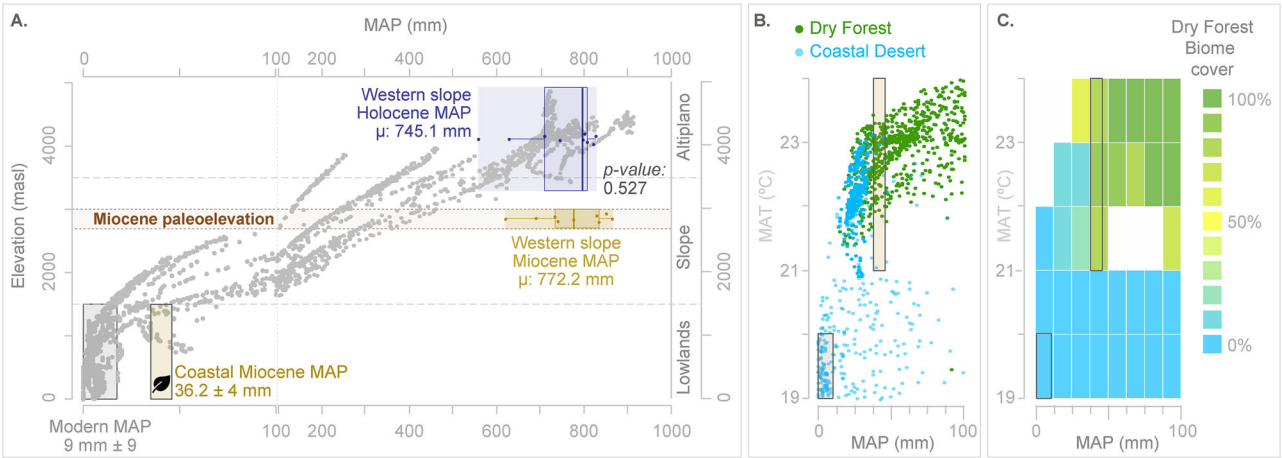

Fig. 4 | Late Miocene and modern climate variability along the central Peruvian coast and slopes (14–16°S). A Altitudinal distribution of modern Mean Annual Precipitation (MAP), indicating lowlands (0–1500 masl), slopes (1500–3500 masl), and altiplano settings (>3500 masl). Brown horizontal bar represents maximum paleoelevation values reconstructed for the Central Andes during the Late Miocene[46,48]. Note change of MAP scale at 100 mm. Boxplots indicate pollen-based western slope MAP estimates during the Late Miocene (yellow) and Holocene (blue). **B** Climate space, defined in terms of MAP (0–100 mm) vs. mean annual temperature (MAT; 19–24 °C), for present-day coastal Peruvian areas classified as belonging to the Dry Forest Biome (green) and Coastal Desert Biome (blue). Biome classification according to the Peruvian National Service for Natural Areas Protected-SERNANP. **C** Proportion of present-day Dry Forest Biome coverage across climate space, estimated on a grid with 10 mm precipitation and 1 °C temperature intervals. Gray and yellow boxes show modern (19–20 °C; 9 ± 9 mm) and Miocene (21–24 °C; 36.2 ± 4 mm) coastal conditions, respectively.

The Miocene palynoflora of the southern Peruvian coast, with its diverse composition, represents a stable, slow-growing community. While its wooded landscape may resemble local riparian floras or dry forest found north of 8°S today[36–38], it features a distinct mix of xerophilous and Andean taxa that are currently not found in association with each other. The co-occurrence of lowland elements, such as *Neltuma*, bombacoids and palms, with abundant modern high-Andean groups, like *Polylepis-Acaena* and *Valeriana*, indicates either a mixed lowland-Andean signal or a biome without a modern analog. Such non-analogy would result from a combination of factors, including shifted ecological habitats and competition due to Miocene atmospheric pCO_2 levels (~400 ppm)[12], different climatic conditions[17], varying pressures from grazing mammals[30,32], plant evolutionary changes, and the lower Andean topography of the Late Miocene[28].

Late Miocene coastal precipitation estimates

We reconstructed mean annual precipitation (MAP) for the Late Miocene Peruvian lowlands using the physiognomic characters of 47 fossil leaves (Supplementary Tables S1–S3; Supplementary Data S5). We tested and refined existing global relationships between leaf size and MAP[39–42], by adding 366 modern leaf specimens representative of the Peruvian coast (Supplementary Table S2). These adjustments made linear models more accurate for hyperarid settings like those in the Peruvian-Chilean region (Supplementary Fig. 6; Supplementary Data S5). We further introduced secondary vein density (2Dv) as an additional measure of leaf size, acknowledging uncertainty in leaf size estimates due to fragmentary fossil material[41,43]. Precipitation reconstruction uncertainty was estimated via Monte Carlo resampling (Supplementary Fig. 6; Supplementary Table S3). The reconstructed Late Miocene MAP value of 36.2 ± 4 (1σ) mm significantly exceeds the historical MAP of 9 mm ± 9 (1σ) (interquartile range (IQ): 3–11 mm) recorded along southern Peruvian lowlands (14–17°S, <1500 masl) (Fig. 4A). The Miocene MAP is even 75% higher than historical maxima of 23.7 mm associated with strong ENSO precipitation events (ENSO mean 9.8 ± 7.0 mm) in the area[44,45]. Comparable MAP values are currently observed above 1500 masl on the western slope of the Andes (Fig. 4B), 30–50 km inland from the present-day coastline (Fig. 4B).

Pollen spectra reflect conditions across a broader spatial scale, including the western Andean flanks. MAP estimates for Miocene and Holocene pollen assemblages were derived using climate envelopes of the nearest living relatives (NLR) of palynomorphs (80 morphotypes, 54.1% of the count) and a quantitative coexistence analysis[46] (see "Methods," Supplementary Data S6–S8; Supplementary Table S4). The pollen-based Miocene MAP was estimated at 772.2 mm ± 81.82 (1σ) (623.5–867.1 mm), slightly higher but not significantly different from the Holocene MAP value of 745.1 mm ± 95.4 (1σ) (558.6–826.2 mm; p value = 0.527). Compared to the Holocene, the Miocene exhibited enhanced seasonal rainfall fluctuations. Rainfall increased significantly during the austral summer rainfall season (p value = 0.003) and decreased during the austral winter (p value = 0.00009; Supplementary Fig. 7). Holocene pollen-derived MAP values are presently observed above 3000 masl in regions covered by grasslands and shrublands[36,38]. In contrast, the amount of Late Miocene precipitation, derived from a wooded-dominated pollen assemblage, is observed today above 3500 masl, but occurred necessarily at a much lower altitude at that time when maximum Andean height was estimated to be around 2800–3000 masl[46–48]. These pollen-based quantifications should be interpreted with caution. In arid environments, plants occupy the drier end of their climatic niche, potentially leading to overestimated rainfall when using their climatic optima. Nevertheless, multiple lines of evidence support the qualitative robustness of our results. Enhanced Andean MAP values are in agreement with Middle to Late Miocene climate reconstructions from the western Chilean Altiplano[49], northern Central Andean Plateau[46], and northern Bolivian Altiplano[50], supporting substantially increased rainfall during the Late Miocene, both on the western slope of the Andes and in the lowlands (Coastal Peruvian Desert), as indicated by fossil pollen and leaves.

Our paleobotanical evidence shows that hyperaridity in the southern Coastal Peruvian Desert, and likely across the Atacama Desert was reduced during the Late Miocene (8–6 Ma), suggesting a later onset of extreme coastal aridity. Indeed, although coeval lowland paleobotanical remains have not been reported yet elsewhere, fossil fauna strongly suggests a similar environment in northern Chile during the Late Miocene. Two crocodilian species, indicative of warm and wet conditions, were common along the Peruvian coast and as far south as 27°S in Chile[51], near the southern limit of the modern Atacama Desert. The Late Miocene coastal marine ecosystems of Peru and Chile, which included aquatic sloths, marine mammals, and mollusks, were similar[52,53], suggesting that the coastal region, from ~12–27°S experienced similar oceanographic and climatic conditions. Our findings provide evidence enabling model-proxy data comparisons for the Coastal Peruvian Desert, which are essential for updating previous vegetation

reconstructions from Global Circulation Models that suggest increased aridity north of 25°S during the Tortonian (~11–7 Ma)[54].

Surplus moisture origin

Three moisture sources may account for additional rainfall in the Coastal Peruvian Desert during the Late Miocene, supporting vegetation expansion and landscape transformation (winter coastal fog, moist air masses advected from the Amazon Basin, and local convection of warm Eastern Tropical Pacific waters). These sources underscore the interplay between coastal landscapes, vegetation dynamics, and atmospheric and oceanic processes linked to the Eastern Tropical Pacific.

Today, winter coastal fogs occur during austral winters along the Peruvian and Chilean coast and are the primary moisture source for "*lomas*" vegetation[36,55] extending from sea level to 1400 m on the Andean foothills. Some Miocene plant genera, such as *Neltuma* and *Capparis*, are indeed typical of these "*lomas,*" potentially representing relicts of ancient vegetation cover. However, fog moisture, favored by cool ocean conditions during the coastal upwelling seasonal maximum, was likely infrequent under the Late Miocene warm climate. In addition to global greenhouse warming, the southeastern tropical Pacific was then 2–4 °C warmer, as a result of a weakened Walker circulation and a reduced East-West sea-surface temperature gradient[56,57].

The second potential source involves westward advection of moist air masses from the Amazon Basin, particularly during the austral summer, when the South American monsoon is active[14,58]. The lower elevation of the Central Andes during the Late Miocene −1.0–1.5 km lower than today[46–48]—could have facilitated this airflow, potentially increasing rainfall and enhancing the western drainage network[16,59]. However, the impact that the Andean uplift imprinted on the aridity of the Peruvian-Chilean coastal region remains debated [e.g., refs.17,27].

The third, and most likely moisture source is local convection in the warm Eastern Pacific. A permanent El Niño-like state for the entire tropical Pacific during the Late Miocene[57,60] has been associated with an El Niño-like precipitation pattern in regions known to be influenced by atmospheric teleconnections across the Tropical Pacific[61]. This means increased precipitation likely occurred on the Peruvian and Chilean coasts, as it occurs today during strong El Niño events[45]. This effect, amplified by higher atmospheric vapor content in a greenhouse climate[62] and increased local evaporation and convection from a shallow-water sea along the southern Peruvian coasts[30,32,33] likely drove the greening of the Coastal Peruvian Desert during the Late Miocene. We consider this mechanism also to be the primary moisture contributor to the western-flowing fluvial drainages.

Climate-driven biome shift, lesson from the past

The Late Miocene species community lacks a modern analog, making vegetation changes best characterized in terms of biome shifts. Modern climatic envelopes, defined using historical climate data from 1970 to 2000, were used to model the range of climatic conditions in which current biomes can persist (See "Methods"). Today, the northern Peruvian coast hosts a dry forest biome (DFB) from 3.4 to 7.8°S, thriving in precipitation ranges from 140 to 305 mm/yr (all climate ranges are given as IQ) and a mean annual temperature (MAT) range of 23–25.3 °C (Fig. 4). The DFB disappears when rainfall drops below 30 mm/yr. The coastal desert biome (CDB), extending from 6.8 to 27°S, exists under a precipitation range of 22–29 mm/yr and MAT of 21.4–22.4 °C (Fig. 4; Supplementary Fig. 9). Between 6.5 and 8°S, a transitional zone emerges, displaying a mosaic of vegetation patches that reflect a southward-decreasing rainfall gradient. Today, the CDB is the sole biome in the Pisco Formation area (Fig. 4B; 13–16.5°S; 0–700 masl), with a MAP of 10 mm (IQ: 2–11 mm) and MAT from 19 to 20 °C[44]. Considering a 2–4 °C temperature increase in the Late Miocene, as indicated by past SST reconstructions[56], and the precipitation range reconstructed from fossil leaves, the coastal climate around the Pisco area covered an expanded climatic space (32–40 mm/yr; 21–24 °C). Based on its modern biome distribution, the likelihood of CDB occurrence in such a climatic space is less than 25% (Fig. 4C). Notably, with 2–4 °C warmer MATs, precipitation would only need to reach 45–60 mm/yr to sustain a permanent wooded greenery, which is consistent with our leaf-based MAP reconstruction (Fig. 4C).

The paleobotanical record reveals that increased rainfall allowed the development of a different continental landscape in the southern Peruvian lowlands. Additional moisture enabled the expansion of a diverse and wooded vegetation, with no present-day analog, supporting sub-xeric to mesic groups, such as *Podocarpus*, *Polylepis-Acaena*, *Neltuma* (ex *Prosopis*), *bombacoids*, palms, and various other taxa (Fig. 5). Such climate conditions facilitated both the southward expansion of the coastal DFB and possibly the survival of Andean groups, such as the *Polylepis-Acaena* clade. This flora then provided sustenance and suitable habitats for a variety of continental mammals (Fig. 5), including the hystricognath rodent *Tetrastylus*, medium-sized macraucheniid litopterns, small marsupials[33], and the carnivoran procyonid *Cyonasua*[63], while warm marine conditions were suitable for sea grass feeders like the aquatic sloth *Thalassocnus*[64].

Climate models simulations of future greenhouse climate consistently predict a circulation change in the tropical Pacific toward El Niño-like mean conditions[62], which, in addition to the global warming trend, may induce a warming of 2–4.5 °C in the Humboldt Current System[65]. The Late Miocene warming is similar, qualitatively and quantitatively, to the projected future warming, and may thus hold the clues to future changes in the hyperarid western South America. Due to high uncertainties in future precipitation regimes worldwide[66], and to the complex interactions between climate, vegetation, and soil moisture[67,68], the future response of vegetation in western South American Desert cannot be robustly predicted. The Late Miocene greening of the coastal desert, however, suggests (i) that changes in the tropical Pacific temperature and dynamics in greenhouse climate conditions may increase convective precipitation and in this region counterbalance the global strengthening of the evaporation-precipitation pattern[1], and (ii) that this increased moisture source may be sustained by climate–vegetation feedbacks. Our results thus support the possibility of an increase in rainfall and vegetation cover in the Peruvian Desert, which, if well managed, may benefit the living conditions of millions.

Methods

Study material and chronology

We recovered 55 leaves, three wood fragments and nine palynological samples from sediments of the coastal to shallow-marine Pisco Formation, that crop out in the AGL Locality within the Sacaco area (15.5°S,74.8°W). The AGL occurs 2 km off the Panamerican Highway and about 10 km east of the village of Puerto Lomas (Supplementary Fig. 1).

The Pisco Formation is interpreted to have been deposited across open or protected shoreface and offshore shelf environments affected by waves and coastal upwelling[30,69]. The succession at AGL consists of alternations of gray and yellow sandstones, locally interbedded with shell banks, chert, and diatomaceous layers. Strata are mostly (sub)horizontal (So = 120/7, n = 20) with little to no structural deformation, resulting in a ~ 200 m-thick composite section[34,70]. The AGL includes five well-known fossiliferous horizons, namely, from oldest to youngest, Pascual, Sirenios, Hueso Blanco, the Water Wells, and Cerro Vildoso[32]. Studied samples were collected from sediments associated with the Hueso Blanco Zone and the Water Wells Zone (Supplementary Figs. 1, 2).

The sedimentary facies associated with the AGL lack any signs of alluvial, fluvial, or estuarine deposits (Supplementary Fig. 2). Sedimentary structures exhibit characteristics consistent with coastal environments, including evidence of bioturbation and sedimentary structures indicative of coastal to shallow-marine settings[33,34,70], such ripple marks, cross-beddings, and occasional hummocky cross-stratification (Supplementary Fig. 2). These features, along with the extensive marine (vertebrate and invertebrate) paleontological record support a depositional environment influenced by marine processes rather than local riverine or alluvial processes[30,32,69,70]. Additionally, there are no relict geomorphological features, such as incised paleovalleys, paleochannels or deltas, that indicate past fluvial transport or riverine incision.

Fig. 5 | Artistic representation of the Central Peruvian coastal landscape during the Late Miocene. This illustration emphasizes the primary floristic components identified in the fossil record, including *Neltuma*, *Podocarpus*, *Salix*, palms, and bombacoids, along with known continental vertebrates, such as the hystricognath rodent *Tetrastylus*, the procyonid *Cyonasua*, marsupials and macraucheniid litopterns. The depiction is intended to convey a generalized view of the landscape rather than a precise reconstruction, as the ecological affinities and habitats of many palynofloral and paleobotanical elements remain unresolved.

The lowermost Pisco strata at the AGL locality have been radiometrically dated as Tortonian (9.2 ± 0.08 Ma; 59), while the uppermost Pisco beds are Messinian in age based on diatom-derived biostratigraphic data (younger than 6.3 Ma but older than 5.6 Ma[70]). Two K-Ar radiometric dates, associated with the guide beds LM6 and LM7 of Brand et al.[34], underlie the leaf-bearing levels and provide a maximum age for the collected material between ~8.8 and 7.9 Ma (samples 44 and 45 in ref.[71]. The youngest age for the studied material is estimated from a U/Pb radiometric age from a 50 cm-thick white ash layer located toward the upper part of the Water Wells Zone, about 5 m below the uppermost pollen sample (6.1 Ma; sample MG6-24; Supplementary Fig. 1).

Palynological analyses

Eighteen palynological samples were studied, nine of Miocene age and nine of Holocene. Miocene pollen samples were retrieved from leaf-bearing levels and upper AGL beds. Five of these samples were collected from the same levels as the macrobotanical remains, while the remaining four were taken from the Water Wells Zone in the AGL (Supplementary Fig. 1).

Holocene samples were used as benchmark of present-day vegetation. Holocene material originates from recent shallow-water sediments from the Paracas Bay and the G-10 gravity core drilled along the Peruvian continental margin[72]. Two samples correspond to the oldest sediments recovered from a 40 cm box core from the Paracas Bay (−13.81, −76.28; water depth: 10 m) dated around 1970–1975 A.D. The remaining seven Holocene samples were collected from the G-10 gravity core (−14.3833; −76.3983; 312 m water depth) during the Galathea-3 expedition[72]. All palynological samples were prepared using standard palynological techniques[73]. Whenever possible, at least 200 palynomorph grains were counted per sample (see Supplementary Data S2).

The final palynological dataset included 4860 occurrences of terrestrial palynomorphs (2413 of Miocene age and 1906 of Holocene age), classified into 288 morphospecies across 18 palynological samples (Fig. 2; Supplementary Data S2). Palynomorphs were identified by referring to regional pollen atlases and reference collections[74–77]. Where possible, updated botanical affinities at the family or genus level were conservatively assigned to the identified palynomorphs using the Rpackage *taxize*[78] (last update 09/2024). After assigning botanical affinities, the identified palynomorphs were categorized into broad taxonomic categories (i.e., angiosperms, gymnosperms, pteridophytes, and unknown ID), by photosynthesis pathway (i.e., C3, C4, CAM, and mixed), and by their growth habit (i.e., arboreal, shrubs, herbs, ferns, and unknown habit; See Supplementary Fig. 3 and Supplementary Data S2).

Diversity and palynofloral composition in comparison with Holocene samples. Standing diversity values per sample were estimated after performing a range-through assumption, and reassessed following elimination of singletons; Fig. S3). Palynofloral standing diversity shows significantly higher diversity values in the Miocene than in the Holocene (Fig. 3A). A similar pattern is observed in within-sample diversity, using rarefied grain counts. At a count of 150 grains (Fig. S3), Miocene samples have a significantly higher number of species (mean = 42.8) compared to those from the Holocene (mean = 28.3, p value = 0.009, df = 6.56). However, the Simpson Index, which assesses the likelihood of randomly selecting two individuals belonging to the same species[79], shows no difference between the Miocene (mean = 0.9) and the Holocene (mean = 0.89, p value = 0.36, df = 11.291), indicating an even distribution of species abundance in both assemblages.

The Chao dissimilarity index (CDI), cluster analysis, and detrended correspondence analyses reveal distinct palynofloral compositions between Miocene and Holocene samples (Fig. 3A, B; Fig. S4). Furthermore, the CDI median between the Miocene and Holocene floras, with a value of 0.49 (Fig. 3D), significantly differs from the within-mean values of the Miocene (0.35; 95% CI [0.2782, 0.4276], p value <0.001) and the Holocene (−0.43; 95% CI [−0.5016, −0.3522], p value <0.001).

Fossil wood anatomy

We collected three wood fragments, two 10 cm silicified pieces from the water wells zone and a 20 cm fragment containing *Teredolites* bioerosion from the leaf-bearing beds (MG8-01; −15.5050, −74.8154; Fig. 2). Transverse, radial longitudinal, and tangential longitudinal petrographic thin sections were prepared from the silicified wood pieces for taxonomic identification.

Taxonomic descriptions followed IAWA terminology and ID numbers[80]. Quantitative characteristics were evaluated measuring a minimum of 25 random vessels per cross and tangential section (Supplementary Data S4). Vessel and ray density were calculated as the average of ten field view samples (at 10 and 20× magnifications. Other anatomical characters, such as ray length or fiber wall thickness, were assessed from ten to 25 random measurements.

A *Neltuma* (ex *Prosopis*) botanical affinity was defined based on results from the inside wood database as follows: ***25p, 30p, 42p, 47p, 66p, 79p, 83p, 98p, 104p, and 143p***[81]. Diagnostic characters observed in the fossil *Neltuma* (ex *Prosopis*) include distinct wood growth rings marked by marginal bands of parenchyma, presenting a diffuse-porous pattern. Solitary vessels with occasional 2–3 radial multiples; simple perforation plates; intervessel pits alternate, ranging from minute to small; non-septate fibers; paratracheal vasicentric, slightly aliform and confluent; non-storied rays, strongly homocellular, and 2–4 seriate, and 2–4 cells per parenchyma strand. Common sclerotic tyloses and prismatic crystals were present and abundant in chambered axial parenchyma cells (Fig. 2; Fig. S5; Supplementary Data S4).

Botanical affinity was compared with *Neltuma* (ex *Prosopis*) and other Fabaceae genera including *Caesalpinia*, *Inga*, *Parkinsonia*, *Senna*, *Tara*, and *Vachelia*, using modern reference samples and photographs from the Inside Wood database. Non-metric multidimensional scaling analyses (Euclidean distance) and cluster analyses (Ward´s method, bootstrap *n*:100) were used to investigate taxonomic distances and relationships between fossil and reference material. A full wood description, taxonomic measurements, and comparisons are provided in Supplementary Data S4. Petrographic thin sections of silicified wood are housed at the Universidad Peruana Cayetano Heredia (Lima, Peru).

Angiosperm leaves

We collected 55 leaf specimens, comprising compressions and impressions, from AGL (MG8-01; −15.505, −74.815). Leaf morphology descriptions follow the terminology of Ellis et al.[82]. No evidence of insect herbivory was observed. Most specimens retained details of leaf shape and venation up to the fourth order ($n = 47$). We determine a few reliable, yet conservative, botanical affinities based on unique foliar characters corresponding to the living family assigned. These affinities are considered conservative estimates due to the limited number of observed characters (Supplementary Data S5). Because of the unresolved taxonomic affinities of the macrofossil material, no floristic composition analysis was performed based on macrofloral remains. Collected leaves are housed at the Universidad Peruana Cayetano Heredia (Lima, Peru). Each specimen retains a collection number using the prefix "MG8-01-XX", where the last two digits represent the specimen number.

MAP estimates based on leaf physiognomic characteristics

Leaf size as MAP predictor. (Method 1—"*observed leaf size*") The natural log of leaf sizes (MlnA) is positively correlated with the natural log of MAP[42,83]. To apply this relation, a summatory of proportional sizes by discrete leaf size categories must be first calculated (MlnA = $\Sigma a_i p_i$). To do so, all dicot specimens are classified into five discrete leaf size categories: leptophyll (<25 mm^2), nanophyll (25–225 mm^2), microphyll (225–2025 mm^2), notophyll (2025–4500 mm^2), and mesophyll (4500–18,225 mm^2). The number of leaves per category is counted, and the leaf size proportion for each category (p_i) is calculated based on these counts. This proportional value is then multiplied by the mean natural log areas (a_i) of the respective five leaf size categories (i.e., a_i: 2.12, 4.32, 6.51, 8.01, and 9.11; see Supplementary Table S1). The resulting values are summed to calculate the mean natural log of leaf size (MlnA = $\Sigma a_i p_i$). MAP estimates are then derived using regional (Tropical Africa-Bolivia, Tropical Africa-Bolivia + (sub)tropical Western Hemisphere[39,42] and global regression models between MlnA and MAP[41].

Vein density as leaf size predictor. (Method 2—"*predicted size*") Estimating leaf sizes from fragments can introduce bias due to incomplete material, potentially leading to errors in the MAP estimation. To mitigate this, we also used 2Dv, a visible trait on the leaf laminae that is correlated with leaf size[84]. This trait allowed us to objectively estimate fossil leaf sizes by calculating mean 2Dv values. When possible, up to three circular regions of known area (a), ranging from 0.023 to 0.1 cm^2, were selected in each laminae to calculate an average 2Dv value per specimen. Each circular region was photographed, and all veins present were manually traced. Their total length (L) was measured using the Topview software, and 2Dv average values were calculated as 2Dv = L/a[85]. The leaf size per specimen (cm^2) was then predicted using the Eq. (1) developed by Sack et al.[43].

$$Ln(\text{leaf area, cm}^2) = 1.96 + 2.04 * \ln(2\text{Dv}) \quad (1)$$

Predicted sizes were used to calculate a new mean natural log of leaf size (MlnA) value as described above, which was subsequently applied to assess MAP values using regional and global equations[39,41,42].

Performance of equations in hyperarid settings. We first evaluated the effectiveness of regional and global equations in estimating present-day MAP values in (hyper) arid environments, acknowledging that extremely low rainfall values may fall at the limit or even outside the range of these equations. For this, we utilized 366 georeferenced modern leaves from 33 coastal species living in xerophytic biomes (i.e., desert and dry forest) along the Peruvian coast (5–1068 masl). Leaf specimens were accessed from the National Herbarium of the Universidad Nacional Mayor de San Marcos in Lima, Peru (Supplementary Data S5). The selection of plant specimens was based on the availability of complete metadata, including taxonomic id, coordinates, altitude, site collection description, as well as the presence of at least ten well-preserved leaves. Sampling excluded individuals that grew in association with natural water bodies (rivers, streams) or in cultivated areas. Of the species sampled, 23 occur in habitats from the central Peruvian region (14–16°S), geographically close to our fossil site. The remaining 11 species belong to the DFB of northern Peru (4–7°S), which exhibits a climatic arid niche, somewhat similar to that of the Central Peruvian coastal region[37]. Leaf sizes and the mean natural log of leaf size (MlnA = $\Sigma a_i p_i$) were calculated using Method 1 (as described above), and modern MAP estimates were obtained again using the mentioned regional and global equations[39,41,42]. These values were then compared to historic MAP data at 5 min resolution (~ 10 km^2) retrieved from the WorldClim database[86]. In all cases, the regression models overestimated modern MAP values, by up to two orders of magnitude (Supplementary Table S2).

Equation recalibration, validation, and testing. To develop a better-fitted regression suitable for (hyper)arid environments, we integrated the modern Peruvian leaf-size data—comprising 366 leaves from 33 species (previously described)—into regional and global regression models[39,41,42]. Although the recalibrated regression models exhibited low *R*-squared values, they still showed significant correlations between Ln (MAP) and Ln (leaf-size) (Supplementary Table S3). The effectiveness of these (hyper) arid-adapted equations was further tested by using a new set of georeferenced leaf-size observations from six species (52 new leaves) retrieved from the Field Museum's online Botanical Collections Database (Fig. S6; Supplementary Data S5). These specimens were also collected from coastal Peruvian settings (8–13°S), and, as in the previous case, did not include individuals collected in proximity to water bodies or cultivated areas. The resulting MAP estimates agreed with historical MAP values retrieved from the WorldClim database (Supplementary Table S2), demonstrating that the (hyper) arid-recalibrated regression models are effective for inferring MAP in extremely dry settings (Fig. S6). Equation 2 describes the best-performing hyperarid-recalibrated regression model (r^2: *0.2332, p value: 1.5e-12*) relating MLnA (=$\Sigma a_i p_i$) and Ln (MAP), which was further used to assess paleoprecipitation estimates.

$$Ln(MAP) = -0.2357015 + 0.3098442 * MLnA \quad (2)$$

Miocene MAP estimates. Miocene MAP values were thus estimated using two methods: observed leaf size (Method 1) and the 2Dv-predicted leaf-size (Method 2). 47 fossil leaves were used for Method 1, while only 36 fossil leaves were used Method 2, as vein density of 11 specimens (out of 47 samples) could not be measured due to their reduced size or poor preservation. Because of this, size of those specimens could only be assessed based on direct observation (Supplementary Table S1).

The best-performing hyperarid-recalibrated regression model (Eq. 2) was used to estimate the Miocene MAP (Supplementary Table S2). However, to consider uncertainty, the final MAP value was calculated by averaging the results obtained from the two methods (Table S3), integrating a bootstrapped value (n = 10,000, utilizing 95% of the data at a time) derived from Method 1 (i.e., direct size observations) with the bootstrapped value derived from Method 2 (i.e., 2Dv-predicted size). The combined result provides a robust estimate of the Miocene MAP by accounting for incompleteness, variability and uncertainty of the fossil data (Fig. S6). Leaf physiognomy, vein density measurements, leaf-derived sizes, and regression models for predicting Ln (MAP) based on leaf size are available in Supplementary Data S5.

MAP based on the climatic tolerance of coexistent NLR of identified palynofloral elements

We estimated pollen-based paleoMAP ranges following the methodology and sample criteria proposed by Martinez et al.[46]. Palynological relative abundances were converted to presence-absence to make Holocene and Miocene samples comparable. Only palynomorphs with known botanical affinities below the family level were chosen for this analysis (Supplementary Data S2). Georeferenced occurrences of the NLR, established based on known taxonomic affinities, were used to define climatic envelopes. Occurrences were retrieved from the BIEN database (downloaded 23/04/2024)[87] using the BIEN *R*-package[88]. Due to the poor representation of biomes in the western Andean lowlands and slopes, occurrences were supplemented with over 37,000 records available in worldwide herbaria and more than 3500 published reports (Supplementary Data S6). Taxonomical status of each added record was reviewed and updated using the *taxize R*-package[78]. Historical climate information (MAP, MAT), and precipitation of the driest and wettest quarters; Supplementary Data S7) for each occurrence was obtained from the WorldClim database, using a 5 min resolution grid[86].

The distribution of taxa with known affinities from the palynological dataset was described through bivariate probability density distributions (PDF) of modern taxon occurrence, using different combinations of the retrieved climatic variables (MAP, MAT, and precipitation of the driest and wettest quarters). Distributions were described through a bivariate Gaussian kernel density estimator (KDE), and reference libraries of bivariate environmental distributions per taxa (48 NLR affinities; see Supplementary Data S7) and temporal groups (Miocene versus Holocene; see Supplementary Data S8) were built. In order to have robust climate probabilities, we generate 100 subsampled KDE´s, each derived from a random 50% subset of the data, to capture variability and reduced noise. PDF retrieved significantly similar MAT and MAP the Miocene and the Holocene; while precipitation estimates for the wettest and driest quarter were found to be significantly different (Fig. S7; Supplementary Table S4). Comparison of Miocene and Holocene MAP values, however, requires caution given reduced Andean elevations during the Late Miocene (1.0–1.5 km lower[46,48]). Nonetheless, as occurs with the leaf physiognomy analysis, the pollen-based MAT estimate suggests enhanced Miocene precipitation.

Climatic envelopes of modern biomes

Climatic biome envelopes were defined based on the modern geographic occurrence of xeric coastal biomes. These envelopes were then used as models to predict the climatic variation range at which biomes can persist. Georeferenced occurrences were extracted from the biome distribution map (Ecoregion shapefile; Ecoregiones_SERNANP.shp) published by the Peruvian National Service for Natural Areas Protected (SERNANP) and used to define climatic envelopes for the DFB and CDB (Fig. S9). The climatic variables of each biome were extracted from the WorldClim database using a 5 min resolution grid[86].

Reporting summary

Further information on research design is available in the Nature Portfolio Reporting Summary linked to this article.

Data availability

All datasets—including (i) U-Pb calculated weighted mean ages, (ii) modern and fossil leaf measurements, (iii) palynological counts, (iv) wood anatomy measurements, (v) Probability density function plots of modern species and fossil samples, and (vi) *R*-source codes—will be made publicly available in the Salamanca University institutional repository portal (GREDOS) at: https://gredos.usal.es/handle/10366/160491.

Code availability

Source code for data treatment is available in R at: https://github.com/Paleoflora/AGL-Miocene.git.

Received: 12 November 2024; Accepted: 22 April 2025;
Published online: 20 May 2025

References

1. Held, I. M. & Soden, B. J. Robust responses of the hydrological cycle to global warming. *J. Clim.* **19**, 5686–5699 (2006).
2. Ortega, C. et al. Extreme ENSO-driven torrential rainfalls at the southern edge of the Atacama Desert during the late holocene and their projection into the 21th century. *Glob. Planet. Change* **175**, 226–237 (2019).
3. Schulz, N., Boisier, J. & Aceituno Gutiérrez, P. Climate change along the arid coast of northern Chile. *Int. J. Climatol.* **32**, 1803–1814 (2011).
4. Tang T., Luo J.-J., Peng K., Qi L. & Tang S. Over-projected Pacific warming and extreme El Niño frequency due to CMIP5 common biases. *Nat. Sci. Rev.* **8**, nwab056 (2021).
5. Capotondi A., Wittenberg A. T., Kug J. S., Takahashi K. & McPhaden M. J. ENSO diversity. In: McPhaden M. J., Santoso A., Cai W. (eds). *El Niño Southern Oscillation in a Changing Climate*, pp. 65–86 (John Wiley & Sons, 2020).
6. Wills, R. C., Dong, Y., Proistosecu, C., Armour, K. C. & Battisti, D. S. Systematic climate model biases in the large-scale patterns of recent sea-surface temperature and sea-level pressure change. *Geophys. Res. Lett.* **49**, e2022GL100011 (2022).
7. Kang, S. M., Shin, Y., Kim, H., Xie, S.-P. & Hu, S. Disentangling the mechanisms of equatorial Pacific climate change. *Sci. Adv.* **9**, eadf5059 (2023).
8. García-Franco, J. L., Gray, L. J. & Osprey, S. The American monsoon system in HadGEM3 and UKESM1. *Weather Clim. Dynam.* **1**, 349–371 (2020).
9. Gouveia, C. D., Rodrigues Torres, R., Marengo, J. A. & Avila-Diaz, A. Uncertainties in projections of climate extremes indices in South America via Bayesian inference. *Int. J. Climatol.* **14**, 7362–7382 (2022).
10. Greve, P. et al. Global assessment of trends in wetting and drying over land. *Nat. Geosci.* **7**, 716–721 (2014).
11. Herbert, T. D. et al. Late Miocene global cooling and the rise of modern ecosystems. *Nat. Geosci.* **9**, 843–847 (2016).
12. Steinthorsdottir, M. et al. The Miocene: the future of the past. *Paleoceanogr. Paleoclimatol.* **36**, e2020PA004037 (2021).
13. Rau, P. et al. Regionalization of rainfall over the Peruvian Pacific slope and coast. *Int. J. Climatol.* **37**, 143–158 (2017).
14. Houston, J. & Hartley, A. J. The central Andean west-slope rainshadow and its potential contribution to the origin of hyper-aridity in the Atacama desert. *Int. J. Climatol.* **23**, 1453–1464 (2003).
15. Takahashi, K. & Battisti, D. S. Processes controlling the mean tropical Pacific precipitation pattern. Part I: The Andes and the eastern Pacific ITCZ. *J. Clim.* **20**, 3434–3451 (2007).

16. Ehlers, T. A. & Poulsen, C. J. Influence of Andean uplift on climate and paleoaltimetry estimates. *Earth Planet. Sci. Lett.* **281**, 238–248 (2009).
17. Sepulchre P., Sloan L. C., Snyder M. & Fiechter J. Impacts of andean uplift on the Humboldt current system: a climate model sensitivity study. *Paleoceanography* **24**, PA4215, 2009.
18. Gayo, E. M. et al. Late Quaternary hydrological and ecological changes in the hyperarid core of the northern Atacama desert (~ 21 S). *Earth-Sci. Rev.* **113**, 120–140 (2012).
19. Ritter, B., Binnie, S. A., Stuart, F. M., Wennrich, V. & Dunai, T. J. Evidence for multiple Plio-Pleistocene lake episodes in the hyperarid Atacama desert. *Quat. Geochronol.* **44**, 1–12 (2018).
20. Baker, P. A. et al. The history of South American tropical precipitation for the past 25,000 years. *Science* **291**, 640–643 (2001).
21. Ritter, B. et al. Neogene fluvial landscape evolution in the hyperarid core of the Atacama desert. *Sci. Rep.* **8**, 13952 (2018).
22. Hoke G. D. et al. Geomorphic evidence for post-10 Ma uplift of the western flank of the central Andes 18 30′–22 S. *Tectonics* **26**, 1–17 2007.
23. Rech, J. A. et al. Massive middle Miocene gypsic paleosols in the Atacama Desert and the formation of the Central Andean rain-shadow. *Earth Planet. Sci. Lett.* **506**, 184–194 (2019).
24. Rech, J. A., Currie, B. S., Michalski, G. & Cowan, A. M. Neogene climate change and uplift in the Atacama Desert, Chile. *Geology* **34**, 761–764 (2006).
25. Reich, M. et al. Supergene enrichment of copper deposits since the onset of modern hyperaridity in the Atacama Desert, Chile. *Miner. Depos.* **44**, 497–504 (2009).
26. Dunai, T. J., López, G. A. G. & Juez-Larré, J. Oligocene–Miocene age of aridity in the Atacama Desert revealed by exposure dating of erosion-sensitive landforms. *Geology* **33**, 321–324 (2005).
27. Hartley, A. J., Chong, G., Houston, J. & Mather, A. E. 150 million years of climatic stability: evidence from the Atacama Desert, northern Chile. *J. Geol. Soc.* **162**, 421–424 (2005).
28. Garreaud, R. D., Molina, A. & Farias, M. Andean uplift, ocean cooling and Atacama hyperaridity: a climate modeling perspective. *Earth Planet. Sci. Lett.* **292**, 39–50 (2010).
29. Jordan, T. E., Kirk-Lawlor, N. E., Blanco, N. P., Rech, J. A. & Cosentino, N. J. Landscape modification in response to repeated onset of hyperarid paleoclimate states since 14 Ma, Atacama Desert, Chile. *GSA Bull.***126**, 1016–1046 (2014).
30. Marocco, R. & Muizon, C. D. Los vertebrados del Neogeno de la costa sur del Perú: ambiente sedimentario y condiciones de fosilización. *Bull. Inst. Fr. d.'études Andi.***17**, 105–117 (1988).
31. Collareta, A. et al. Vertebrate palaeoecology of the pisco formation (Miocene, Peru): glimpses into the ancient Humboldt current ecosystem. *J. Mar. Sci. Eng.* **9**, 1188 (2021).
32. Muizon, C. D. & DeVries, T. J. Geology and paleontology of late Cenozoic marine deposits in the Sacaco area. *Geol. Rundsch.* **74**, 547–563 (1985).
33. Ochoa, D. et al. Late Neogene evolution of the Peruvian margin and its ecosystems: a synthesis from the Sacaco record. *Int. J. Earth Sci.* **110**, 995–1025 (2021).
34. Brand, L., Urbina, M., Chadwick, A., DeVries, T. J. & Esperante, R. A high resolution stratigraphic framework for the remarkable fossil cetacean assemblage of the Miocene/Pliocene pisco formation, Peru. *J. South Am. Earth Sci.* **31**, 414–425 (2011).
35. Kuentz, A., De Mera, A. G., Ledru, M. P. & Thouret, J. C. Phytogeographical data and modern pollen rain of the puna belt in southern Peru. *J. Biogeogr.* **34**, 1762–1776 (2007).
36. Rundel, P. W. et al. The phytogeography and ecology of the coastal Atacama and Peruvian deserts. *Aliso A J. Syst. Evol. Bot.* **13**, 1–49 (1991).
37. Whaley, O. Q., Orellana-Garcia, A. & Pecho-Quispe, J. O. An annotated checklist to vascular flora of the ica region, Peru—with notes on endemic species, habitat, climate and agrobiodiversity. *Phytotaxa* **389**, 1–125 (2019).
38. Sarmiento, G. The dry plant formations of South America and their floristic connections. *J. Biogeogr.* **2**, 233–251 (1975).
39. Gregory-Wodzicki, K. M. Relationships between leaf morphology and climate, Bolivia: implications for estimating paleoclimate from fossil floras. *Paleobiology* **26**, 668–688 (2000).
40. Jacobs, B. F. & Herendeen, P. S. Eocene dry climate and woodland vegetation in tropical Africa reconstructed from fossil leaves from northern Tanzania. *Palaeogeogr. Palaeoclimatol. Palaeoecol.* **213**, 115–123 (2004).
41. Peppe D. J., Baumgartner A., Flynn A. & Blonder B. Reconstructing paleoclimate and paleoecology using fossil leaves. *Methods in Paleoecology: Reconstructing Cenozoic Terrestrial Environments and Ecological Communities,* 289–317 (Springer Int. Publishing, 2018).
42. Wilf, P., Wing, S. L., Greenwood, D. R. & Greenwood, C. L. Using fossil leaves as paleoprecipitation indicators: an eocene example. *Geology* **26**, 203–206 (1998).
43. Sack, L. et al. Developmentally based scaling of leaf venation architecture explains global ecological patterns. *Nat. Commun.* **3**, 837 (2012).
44. Senamhi. Datos Hidrometeorológicos a nivel nacional. Lima, Peru ed. (National Service of Meteorology and Hydrology of Peru, 2023).
45. Tapley, J.rT. D. & Waylen, P. R. Spatial variability of annual precipitation and ENSO events in western Peru. *Hydrol. Sci. J.* **35**, 429–446 (1990).
46. Martínez, C. et al. Neogene precipitation, vegetation, and elevation history of the Central Andean plateau. *Sci. Adv.* **6**, eaaz4724 (2020).
47. Garzione, C. N. et al. Tectonic evolution of the Central Andean plateau and implications for the growth of plateaus. *Annu. Rev. Earth Planet. Sci.* **45**, 529–559 (2017).
48. Kar, N. et al. Rapid regional surface uplift of the northern Altiplano plateau revealed by multiproxy paleoclimate reconstruction. *Earth Planet. Sci. Lett.* **447**, 33–47 (2016).
49. Mentzer, C. et al. Late Miocene-early Pliocene hydroclimate evolution of the western Altiplano, northern Chile: Implications for aridification trends under warming climate conditions. *Glob. Planet. Change* **245**, 104674 (2025).
50. Gregory-Wodzicki, K. M. A Late Miocene subtropical-dry flora from the northern Altiplano, Bolivia. *Palaeogeogr. Palaeoclimatol. Palaeoecol.* **180**, 331–348 (2002).
51. Salas-Gismondi, R. et al. Miocene fossils from the southeastern Pacific shed light on the last radiation of marine crocodylians. *Proc. R. Soc. B* **289**, 20220380 (2022).
52. Vermeij, G. J. et al. The temperate marine Peruvian Province: How history accounts for its unusual biota. *Ecol. Evol.***14**, e70048 (2024).
53. Canto, J., Yáñez, J. & Rovira, J. Estado actual del conocimiento de los mamíferos fósiles de Chile. *Estudios Geol.***66**, 255–284 (2010).
54. Pound, M. J. et al. A Tortonian (Late Miocene, 11.61–7.25 Ma) global vegetation reconstruction. *Palaeogeogr. Palaeoclimatol. Palaeoecol.* **300**, 29–45 (2011).
55. Gonzales, F. N., Craven, D. & Armesto, J. J. Islands in the mist: A systematic review of the coastal lomas of South America. *J. Arid Environ.* **211**, 104942 (2023).
56. Dekens P. S., Ravelo A. C. & McCarthy M. D. Warm upwelling regions in the Pliocene warm period. *Paleoceanography* **22**, PA001394, (2007).
57. Wara, M. W., Ravelo, A. C. & Delaney, M. L. Permanent El Niño-like conditions during the Pliocene warm period. *Science* **309**, 758–761 (2005).
58. Garreaud, R., Vuille, M. & Clement, A. C. The climate of the Altiplano: observed current conditions and mechanisms of past changes. *Palaeogeogr. Palaeoclimatol. Palaeoecol.* **194**, 5–22 (2003).

59. Insel, N., Poulsen, C. J., Ehlers, T. A. & Sturm, C. Response of meteoric δ18O to surface uplift—Implications for Cenozoic Andean plateau growth. *Earth Planet. Sci. Lett.* **317**, 262–272 (2012).
60. Ravelo, A. C., Andreasen, D. H., Lyle, M., Lyle, A. O. & Wara, M. W. Regional climate shifts caused by gradual global cooling in the Pliocene epoch. *Nature* **429**, 263–267 (2004).
61. Molnar, P. & Cane, M. A. El Niño's tropical climate and teleconnections as a blueprint for pre-Ice Age climates. *Paleoceanography* **17**, 11–11 (2002). 11-11.
62. Cai, W. et al. Changing El Niño–Southern oscillation in a warming climate. *Nat. Rev. Earth Environ.* **2**, 628–644 (2021).
63. Tarquini, J., Soibelzon, L. H., Salas-Gismondi, R. & Muizon Cd. Cyonasua (Carnivora, Procyonidae) from late Miocene of Peru shed light on the early dispersal of carnivorans in South America. *J. Vertebr. Paleontol.* **40**, e1834406 (2020).
64. Mcdonald, H. G. & Muizon Cd. The cranial anatomy of Thalassocnus (Xenarthra, Mammalia), a derived nothrothere from the neogene of the pisco formation (Peru). *J. Vertebr. Paleontol.* **22**, 349–365 (2002).
65. Echevin, V. et al. Physical and biogeochemical impacts of RCP8. 5 scenario in the Peru upwelling system. *Biogeosciences* **17**, 3317–3341 (2020).
66. IPCC. Climate change 2023: synthesis report. contribution of working groups I, II and III to the sixth assessment report of the intergovernmental panel on climate change [Core Writing Team, H. Lee and J. Romero (eds.)] pp. 35–115 (IPCC, 2023).
67. Lian, X. et al. Multifaceted characteristics of dryland aridity changes in a warming world. *Nat. Rev. Earth Environ.* **2**, 232–250 (2021).
68. Abel, C., Abdi, A. M., Tagesson, T., Horion, S. & Fensholt, R. Contrasting ecosystem vegetation response in global drylands under drying and wetting conditions. *Glob. Change Biol.* **29**, 3954–3969 (2023).
69. Dunbar, R. B., Marty, R. C. & Baker, P. A. Cenozoic marine sedimentation in the Sechura and Pisco basins, Peru. *Palaeogeogr. Palaeoclimatol. Palaeoecol.* **77**, 235–261 (1990).
70. Ochoa, D. et al. Age and provenance of the Mio-Pleistocene sediments from the Sacaco area, Peruvian continental margin. *J. South Am. Earth Sci.* **116**, 103799 (2022).
71. Muizon, C. D. & Bellon, H. Nouvelles données sur l'âge de la Formation Pisco (Pérou). *C*. r. hebd. séances Acad. sci. **303**, 1401–1404 (1986).
72. Salvatteci, R. et al. The response of the Peruvian upwelling ecosystem to centennial-scale global change during the last two millennia. *Climate* **10**, 715–731 (2014).
73. Traverse A. *Paleopalynology*, 2nd edn. (Springer Dordrecht, 2007).
74. Heusser C. J. *Pollen and spores of Chile: Modern types of the Pteridophyta, Gymnospermae, and Angiospermae*, 1st edn. (The Univ. Arizona, 1971).
75. Jaramillo C. & Rueda M. A Morphological Electronic Database of Cretaceous-Cenozoic and Extant pollen, spores and dinoflagellates from Northern South America. 2024 [cited 2024]Available from: http://biogeodb.stri.si.edu/jaramillosdb/web/morphological.
76. Morales C. Palinología de la Flora Actual del Refugio de Vida Silvestre Los Pantanos de Villa (Lima-Perú). Lic. en Biología thesis (Universidad Nacional Federico Villarreal, 2015).
77. Tejada-Fajardo, A., Montenegro, J.-F., La Torrre, M., Orosco, B. & Ochoa, D. Palynological characterization of a seasonal desertic ecosystem: The Peruvian Lomas. *Palynology* **49**, 2396003 (2024).
78. Chamberlain S. et al. R Package ''taxize." *Taxonomic Information from Around the Web*. 0.9.98 ed: R package; 2020.
79. Hill, M. O. Diversity and evenness: a unifying notation and its consequences. *Ecology* **54**, 427–432 (1973).
80. Wheeler, E. A. Insidewood—a web resource for hardwood identification. *IAWA J.* **32**, 199–211 (2011).
81. Wheeler, E. A., Baas, P. & Gasson, P. E. IAWA list of microscopic features for hardwood identification. *IAWA J.* **10**, 219 (1989).
82. Ellis B. et al. *Manual of Leaf Architecture* (Cornell Univ. Press, 2009).
83. Webb L. J. A physiognomic classification of Australian rain forests. *J. Ecol.* **47**, 551–570 (1959).
84. Peppe, D. J. et al. Sensitivity of leaf size and shape to climate: global patterns and paleoclimatic applications. *N. Phytol.***190**, 724–739 (2011).
85. Uhl, D. & Mosbrugger, V. Leaf venation density as a climate and environmental proxy: a critical review and new data. *Palaeogeogr. Palaeoclimatol. Palaeoecol.* **149**, 15–26 (1999).
86. Fick, S. E. & Hijmans, R. J. WorldClim 2: new 1-km spatial resolution climate surfaces for global land areas. *Int. J. Climatol.* **37**, 4302–4315 (2017).
87. Enquist, B. The botanical information and ecology network: cyberinfrastructure for an integrated botanical information network to investigate the ecological impacts of global climate change on plant biodiversity. *PeerJ.* **4**, e2615v2612 (2016).
88. Maitner, B. S. et al. The BIEN R package: a tool to access the botanical information and ecology network database. *Methods Ecol. Evol.***9**, 373–379 (2018).

Acknowledgements

We thank S.S. (UPCH, Peru) for logistical assistance and several Peruvian students for field and lab support (B.O., K.Q., and A.T.). Sincere appreciation to GCO for guidance on new language tools. This project has received funding from the European Union's Horizon 2020 research and innovation program under the Marie Skłodowska-Curie grant agreement No. 101034371 (D.O.), the CONCYTEC-PROCIENCIA research grant awarded to D.O. (No. PE501078563-2022-PROCIENCIA) and through the *Programa de incorporación de investigadores* awarded to J.C. and M.C. (Grant No. E034-2019-02-FONDECYT-BM), and the Ministerio de Ciencia, Innovación y Universidades (Spain) PICTURE Project PID2021-128322NB-I00 (J.A.F.). Samples were collected under sampling permit No. 125-2018/DGPA/VMPCIC/MC (Lima, April 6, 2018), issued to M.C. and R.S.G.

Author contributions

D.O. and M.C. conceptualized and led the writing of the study. J.F.M., T.D.V., F.Q., R.S.-G., and M.U. were involved in the field methodology. D.O., J.F.M., D.C.-R., and O.R.-R. conducted the paleobotanical data analysis (pollen, leaves, and wood anatomy). D.O., J.F.M., and M.L.-A. gathered and identified modern herbarium data (leaves). F.Q., A.B.-E., D.C., and D.F. performed geochemical analyses and radiometric dating. E.C.-A., and P.R., contributed with statistical analyses. D.O., J.A.F., M.R.-C., J.C., and M.C. worked on funding acquisition. All authors contributed to the writing, review, and editing of the manuscript.

Competing interests

The authors declare no competing interests.

Additional information

Supplementary information The online version contains supplementary material available at https://doi.org/10.1038/s43247-025-02322-0.

Correspondence and requests for materials should be addressed to Diana Ochoa.

Peer review information *Communications Earth & Environment* thanks *Liang Xiao, Carina Hoorn* and the other, anonymous, reviewer(s) for their contribution to the peer review of this work. Primary Handling Editor: Alice Drinkwater. A peer review file is available.

Reprints and permissions information is available at http://www.nature.com/reprints

Publisher's note Springer Nature remains neutral with regard to jurisdictional claims in published maps and institutional affiliations.

Open Access This article is licensed under a Creative Commons Attribution-NonCommercial-NoDerivatives 4.0 International License, which permits any non-commercial use, sharing, distribution and reproduction in any medium or format, as long as you give appropriate credit to the original author(s) and the source, provide a link to the Creative Commons licence, and indicate if you modified the licensed material. You do not have permission under this licence to share adapted material derived from this article or parts of it. The images or other third party material in this article are included in the article's Creative Commons licence, unless indicated otherwise in a credit line to the material. If material is not included in the article's Creative Commons licence and your intended use is not permitted by statutory regulation or exceeds the permitted use, you will need to obtain permission directly from the copyright holder. To view a copy of this licence, visit http://creativecommons.org/licenses/by-nc-nd/4.0/.

© The Author(s) 2025